SUPPLEMENTARY INFORMATION

doi:10.1038/nature09568

Contents

I. EXPERIMENTAL PROCEDURES FOR MATTER-LIGHT QUANTUM INTERFACE

As shown in Fig. S1a, we split a write pulse into four beams with two calcite beam-displacers $\{\mathrm{BD}_1, \mathrm{BD}_2\}$, with output fields of the form $\vec{E}_{\text{write}} = (\vec{E}_a + e^{i\phi_1^{(w)}}\vec{E}_b) + e^{i\phi_2^{(w)}}(\vec{E}_c + e^{i\phi_3^{(w)}}\vec{E}_d)$. We control their relative intensities using the two waveplates $(\lambda/2)$ near $\{\mathrm{BD}_1, \mathrm{BD}_2\}$, with writing phases $\phi_i^{(w)} \in \{\phi_1^{(w)}, \phi_2^{(w)}, \phi_3^{(w)}\}$ set by the tilting angles of $\{\mathrm{BD}_1, \mathrm{BD}_2\}$. In turn, the heralding fields $\gamma_1 = \{a_1, b_1, c_1, d_1\}$ emitted from the writing process are combined into two spatial modes at BD_3, with each mode carrying polarizations $\{|H\rangle, |V\rangle\}$ to accommodate the fields $\gamma_1^{(ab)} = \{a_1, b_1\}$ and $\gamma_1^{(cd)} = \{c_1, d_1\}$. We then interfere the polarization components of the spatial modes $\{\gamma_1^{(ab)}, \gamma_1^{(cd)}\}$ by way of BD_4, whose output modes experience polarization interference at the polarizing beamsplitter PBS_h, with one output monitored by the heralding detector D_h. Here, the relative phases acquired by the propagation of fields γ_1 before the detection at D_h are given by $\phi_i^{(h)} \in \{\phi_1^{(h)}, \phi_2^{(h)}, \phi_3^{(h)}\}$. We control $\phi_i^{(h)}$ with a set of Berek compensators.

A photoelectric detection of a single photon γ_1 emitted indistinguishably by one of four ensembles $\epsilon = \{a, b, c, d\}$ prepares an atomic entangled state $\hat{\rho}_W^{(A)}$, whose mutual phases $\phi_i \in \{\phi_1, \phi_2, \phi_3\}$ between ensembles $\{a, b\}$, $\{a, c\}$, and $\{c, d\}$ are $\phi_i = \phi_i^{(w)} - \phi_i^{(h)}$ for $i \in \{1, 2, 3\}$. To generate a 'crossed' quantum state $\hat{\rho}_\times^{(A)}$, we replace PBS_h with a non-polarizing beamsplitter BS_h in the heralding interferometer (Fig. S1a), such that the fields $\gamma_1^{(ab)}$ and $\gamma_1^{(cd)}$ are mixed with orthogonal polarizations. While in practice we do not discriminate events arising from the fields $\gamma_1^{(ab)}$ and $\gamma_1^{(cd)}$, the intrinsic possibility of analyzing the polarization state of the heralding photon to infer the two distinct events completely destroys the bipartite coherence (and entanglement) for the split between $\{a, b\}$ and $\{c, d\}$.

Finally, after a variable delay, a strong counter-propagating read pulse, with reading phases $\phi_i^{(r)} \in \{\phi_1^{(r)}, \phi_2^{(r)}, \phi_3^{(r)}\}$ set by $\{\mathrm{BD}_3, \mathrm{BD}_4\}$, transforms the entangled atomic components $\{a, b, c, d\}$ of $\hat{\rho}_W^{(A)}$ to entangled beams $\gamma_2 = \{a_2, b_2, c_2, d_2\}$ comprising the photonic state $\hat{\rho}_W^{(\gamma)}$. The photonic phases $\{\phi_1', \phi_2', \phi_3'\}$ of $\hat{\rho}_W^{(\gamma)}$ depend on the overall accumulation of atomic phases ϕ_i via $\phi_i' = \phi_i^{(r)} - \phi_i$. Importantly, the set of calcite displacers $\{\mathrm{BD}_1, \mathrm{BD}_2, \mathrm{BD}_3, \mathrm{BD}_4\}$ forms an interferometrically stable four-mode Mach-Zehnder device, in which any common-mode phase drift of $\{\phi_i^{(w)}, \phi_i^{(r)}, \phi_i^{(h)}, \phi_i'\}$ is passively counter-balanced over several days. Thus, the entangled state $\hat{\rho}_W^{(A)}$ $(\hat{\rho}_W^{(\gamma)})$ in our experiment[1] is generated with stable phases $\{\phi_1, \phi_2, \phi_3\}$ $(\{\phi_1', \phi_2', \phi_3'\})$ from trial to trial, which can be transferred to independent reference frames for entanglement verification without exploiting additional quantum channels[2].

II. OPERATIONAL PROCEDURES FOR ENTANGLEMENT VERIFICATION

To verify the entanglement of the photonic state $\hat{\rho}_W^{(\gamma)}$, we use a nonlocal, nonlinear uncertainty relation[4], in which mode-entangled states for $M > 2$ can be efficiently detected with a significantly smaller number of measurements than conventional techniques[4,5]. Specifically, our protocol requires measurements of (U) the photon statistics y_c and (L) the mutual coherences Δ of the multipartite entangled optical modes, as shown in Fig. S1b.

---

† Present address : National Institute of Standards and Technology, Boulder, Colorado 80305, USA

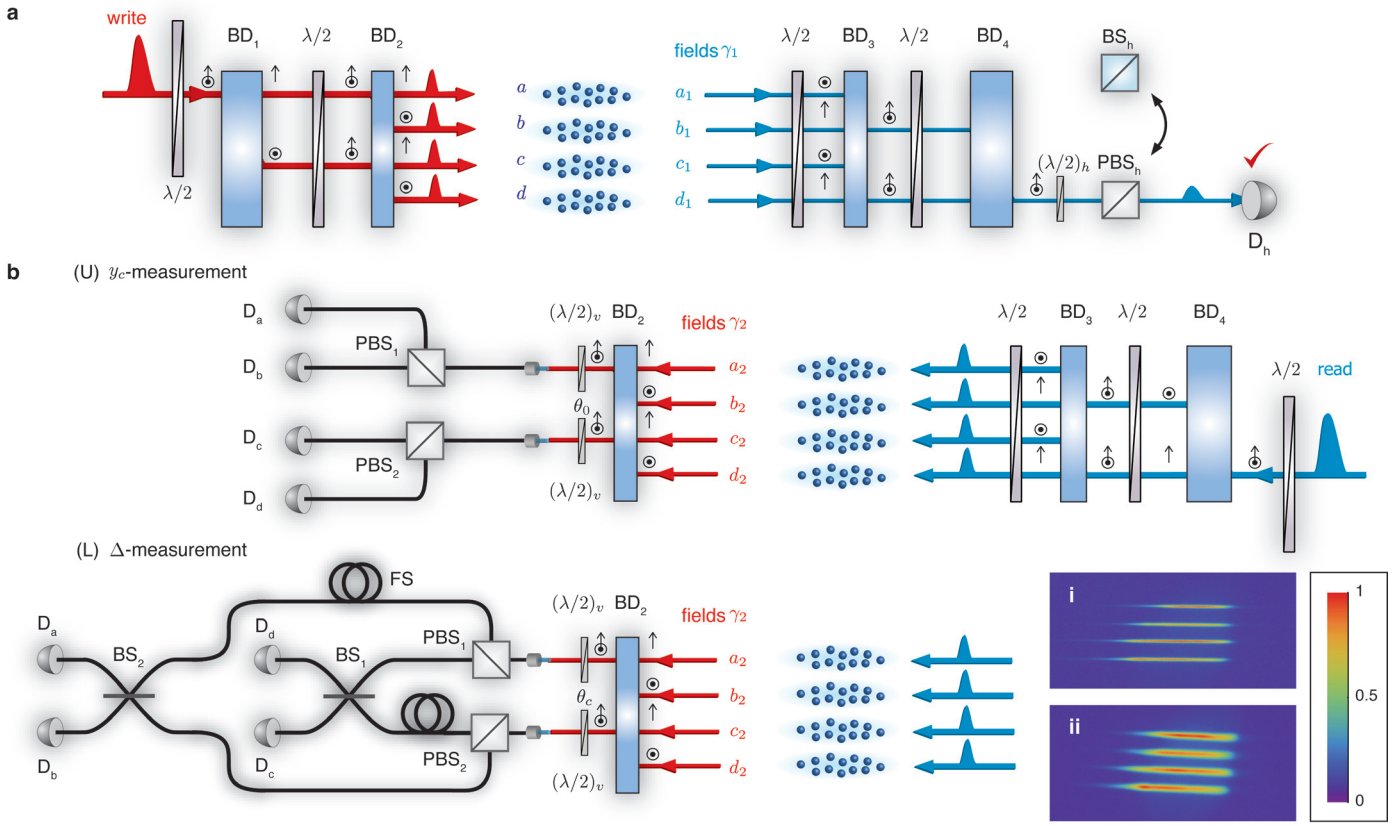

FIG. S1 **Experimental schematics for entanglement generation, transfer, and verification. a,** Entanglement generation. A weak write laser is sequentially split into four components by displacers $\{\mathrm{BD}_1, \mathrm{BD}_2\}$ to excite atomic ensembles $\epsilon = \{a, b, c, d\}$. The resulting fields $\gamma_1 = \{a_1, b_1, c_1, d_1\}$ are brought into interferences with displacer BD_4 and polarizing beamsplitter PBS_h, and sent to a single-photon detector D_h. A detection event at D_h heralds the creation of a quadripartite entangled state. **b,** Quantum-state transfer and entanglement verification. After a storage time τ, we convert the atomic state of the ensembles $\epsilon = \{a, b, c, d\}$ to an entangled state for fields $\gamma_2 = \{a_2, b_2, c_2, d_2\}$ by way of strong read pulses. (U) y_c-measurement – By setting the waveplates $(\lambda/2)_v$ to $\theta_0 = 0°$, we measure the occupation statistics of the individual modes with detectors $D_{a,b,c,d}$. (L) Δ-measurement – With $(\lambda/2)_v$ at $\theta_c = 22.5°$, we optimize the verification phases $\{\beta_1, \beta_2, \beta_3\}_v$ for constructive interferences of the fields γ_2 at $\mathrm{PBS}_{1,2}$ and $\mathrm{BS}_{1,2}$. Piezoelectric fiber stretching modules (FS) are used in the verification interferometer for active stabilizations of $\{\beta_1, \beta_2, \beta_3\}_v$. The quadripartite atomic entanglement is generated for four collective atomic modes of the ensembles $\epsilon = \{a, b, c, d\}$ in inset (i), which are individually controlled by the classical writing, repumping, and reading lasers shown in inset (ii). Both images in the insets (i), (ii) result from background-subtracted fluorescences of the four atomic ensembles. The quantum fields $\{\gamma_1, \gamma_2\}$ are generated in a non-collinear geometry[3] with a crossing angle of 2.5° (not shown) relative to the classical beams.

Operationally, we measure the entanglement parameters by first combining the four optical modes $\gamma_2 = \{a_2, b_2, c_2, d_2\}$ with BD_2 into two spatial modes $\gamma_2^{(ab)} = \{a_2, b_2\}$ and $\gamma_2^{(cd)} = \{c_2, d_2\}$, with each mode $\{a_2, b_2\}$ ($\{c_2, d_2\}$) of γ_2 encoded in the respective polarizations $\{|H\rangle, |V\rangle\}$ of $\gamma_2^{(ab)}$ ($\gamma_2^{(cd)}$). By rotating two waveplates $(\lambda/2)_v$ before $\mathrm{PBS}_{1,2}$ between $\theta_0 = 0°$ and $\theta_c = 22.5°$, and by reconfiguring the fiber-optical connections, we switch between the measurement setups for accessing y_c and Δ.

In particular, measuring the sum uncertainty Δ involves pairwise interference of the optical channels $\gamma_2 = \{a_2, b_2, c_2, d_2\}$. The coherence properties of the photonic state are characterized by the stable photonic phases of $\{\phi_1', \phi_2', \phi_3'\}$, and by the off-diagonal elements $d_{\alpha\beta}$ of $\hat{\rho}_W^{(\gamma)}$ (Methods). This requires high phase stability of $\{\beta_1, \beta_2, \beta_3\}_v$ for the relative optical paths of the verification interferometer shown in Fig. S1b. Here, $\{\beta_1, \beta_2, \beta_3\}_v$ denote to the relative phases between the modes $\{a_2, b_2\}$, $\{a_2, c_2\}$, and $\{c_2, d_2\}$, respectively. Additionally, $\{\beta_1, \beta_2, \beta_3\}_v$ of each optical path leading from the output faces of the ensembles must be tuned to $\{\phi_1', \phi_2', \phi_3'\}$ such that maximum constructive interferences for the fields $\{a_2, b_2, c_2, d_2\}$ occur in a pairwise and sequential fashion[5]. We achieve the optimal settings of these phases by varying $\{\beta_1, \beta_2, \beta_3\}_v$ and recording the sum uncertainty. Fig. 2a in the main experiment[1] shows such a measurement for β_2.

To stabilize the verification phases $\{\beta_1, \beta_2, \beta_3\}_v$, we incorporated an auxiliary reference laser $\vec{E}_{\mathrm{aux}}$ to probe the interferometer during the laser cooling and trapping stage of our experiment via an *ex-situ* phase modulation spectroscopy[5]. The active sta-

bilizations of $\{\beta_1, \beta_2, \beta_3\}_v$ rely upon the passively stable paths of the eight quantum fields $\{\gamma_1, \gamma_2\}$.

During the phase stabilization stage, the outputs of the verification interferometer are routed to a set of auxiliary photodetectors by micro-electromechanical switches (MEMS) to monitor $\{\beta_1, \beta_2, \beta_3\}_v$. We also use another set of MEMS for switching $\vec{E}_{\text{aux}}$, which can extinguish the intensity of the reference laser with an overall extinction of $\gtrsim 200$ dB during the operation of the quantum interface. Additionally, by setting the frequency of $\vec{E}_{\text{aux}}$ to the $|s\rangle - |e\rangle$ transition of Caesium, $\vec{E}_{\text{aux}}$ initializes the ensembles $\epsilon = \{a, b, c, d\}$ to the ground state $|g\rangle$ of the quantum interface. Based on the interference signal of $\vec{E}_{\text{aux}}$, we apply a feedback signal to the two piezoelectric fiber stretching modules (FS) in Fig. S1 that control the relative path lengths (β_2) leading from the ensembles. The remaining phases $\{\beta_1, \beta_3\}_v$ are passively stabilized by stable interferometers (over several days), and controlled independently with a set of calcite Berek compensators.

To operate the quantum interface (3 ms), (i) we set the control signals for the fiber stretchers to values $V_0 + V_c$, with set-point V_0 corresponding to a fixed phase β_2 of the interferometer during stabilization, (ii) switch off the laser $\vec{E}_{\text{aux}}$, and (iii) reroute the interferometer outputs to the single-photon counters $D_{a,b,c,d}$ via the MEMS for 3 ms. This system allows to set the phases β_2 to an arbitrary value by incrementing V_0 by V_c to $V_0 + V_c$, with no degradation for the quantum statistics and coherence of $\hat{\rho}_W^{(\gamma)}$. Moreover, the verification phases remain stable for the 3-ms operating duration of the quantum interface. Thus, the asynchronous (*'ex-situ'*) sequences for acquiring and stabilizing $\{\beta_1, \beta_2, \beta_3\}_v$ of the verification interferometer do not affect the sensitive operation of the quantum interface. In addition, the asynchronous timings allow the generation process of the atomic (photonic) entanglement with atomic (photonic) phases $\{\phi_1, \phi_2, \phi_3\}$ ($\{\phi_1', \phi_2', \phi_3'\}$) to be independent of the procedures for stabilizing the verification phases $\{\beta_1, \beta_2, \beta_3\}_v$, thereby satisfying the entanglement verification criteria of ref.[2].

III. NUMERICAL OPTIMIZATIONS OF THE UNCERTAINTY BOUNDS AND THEIR ERRORS

In the presence of technical imperfections in the verification interferometer arising from imbalances in transmission losses $\{\eta, \eta'\}$ and beamsplitting ratios $\{\alpha, \alpha'\}$ of Fig. S2, the ideal projectors $\hat{\Pi}_i^{(c)} = |W_i\rangle_v\langle W_i|$ evolve into modified sets $\hat{\pi}_i^{(c)} = |W_i'\rangle_v\langle W_i'|$, which project the input $\hat{\rho}_r$ onto imbalanced W-states $|W_i'\rangle_v$, with refs.[4,5] providing further details. Generally, these projectors $\hat{\pi}_i^{(c)}$ are non-orthonormal due to the differential losses, but still span the single-excitation subspace $\hat{\rho}_1$ of $\hat{\rho}_r$. Importantly, the reductions of projection fidelities $F_i^{(\pi)} = {}_v\langle W_i|\hat{\pi}_i^{(c)}|W_i\rangle_v \leq 1$ of $\hat{\pi}_i^{(c)}$ can only decrease the *efficacy* of the verification protocol for detecting larger sets of states that belong to the state space of genuine W-states. Therefore, the observation of Δ below the bounds $\Delta_b^{(M-1)}$ using the modified projectors is still a sufficient condition for genuine M-partite

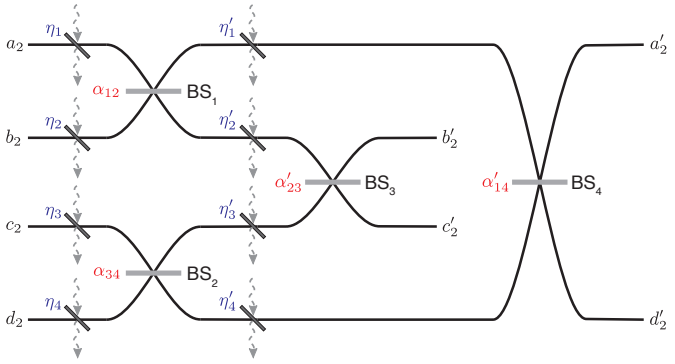

FIG. S2 **Various imperfections in verification interferometer.** The verification interferometer transforms the input photonic modes $\gamma_2 = \{a_2, b_2, c_2, d_2\}$ to the output modes $\gamma_2' = \{a_2', b_2', c_2', d_2'\}$. The projectors $\hat{\Pi}_i^{(c)}$ are transformed into imbalanced states $\hat{\pi}_i^{(c)}$ due to losses and imbalances in the verification protocol. The transmission efficiencies $\{\eta, \eta'\}$ (blue) and beamsplitting ratios $\{\alpha, \alpha'\}$ (red) are shown. Dashed arrows are the auxiliary modes for loss propagations of the input state $\hat{\rho}_W^{(\gamma)}$.

entanglement[4]. In the experiment[1], the losses and beamsplitter ratios for the interferometer are matched within 5%, as shown in Table I.

To quantify the accuracies of our projectors $\pi_i^{(c)}$ to those of an ideal Δ-measurement, we numerically simulate the projection fidelities $F_i^{(\pi)}$ of the modified $\hat{\pi}_i^{(c)}$, as implemented by the measurement apparatus in Fig. S1b, to the ideal $\hat{\Pi}_i^{(c)}$. For this, we assume normal distributions for the parameters in Table I due to their systematic uncertainties, and build histograms of $F_i^{(\pi)}$ in Fig. S3, which give the probability densities $p_d(F_i^{(\pi)})$ for $F_i^{(\pi)}$ such that $\int_0^1 p_d dF_i^{(\pi)} = 1$. Due to the quadratic structure of the projection fidelities, $F_i^{(\pi)}$ is insensitive to small variations in the parameters of Table 1 when the verification interferometer is close to balanced (i.e. $\alpha_{12} \simeq \alpha_{34} \simeq \alpha_{14}' \simeq \alpha_{23}' \simeq 1/2$, $\eta_1 \simeq \eta_2 \simeq \eta_3 \simeq \eta_4$, and $\eta_1' \simeq \eta_2' \simeq \eta_3' \simeq \eta_4'$). Thus, we find a mean value $F^{(\pi)}$ of the four projection fidelities with $F^{(\pi)} = \frac{1}{4}(F_a^{(\pi)} + F_b^{(\pi)} + F_c^{(\pi)} + F_d^{(\pi)}) = 99.9^{+0.1}_{-0.2}$ % by fitting the resulting probability densities $p_d^{(i)}$ to asymmetric Gaussian distributions $G(F_i^{(\pi)})$. The close-to-unity $\{F_i^{(\pi)}\}$ justify our analysis of the entanglement fidelities $\{F^{(A)}, F^{(\gamma)}\}$ for the atomic and photonic states in ref.[1].

In addition, we extend this model to numerically minimize the uncertainty bounds $\{\Delta_b^{(3)}, \Delta_b^{(2)}, \Delta_b^{(1)}\}$ over the full range of y_c for tripartite, bipartite entangled states, and for fully separable states, respectively[4,5]. The calibration errors in the parameters of Table I give rise to the bands in the uncertainty bounds of Figs. 2 and 3 in the experiment[1], which depict the ± 1 s.d. uncertainties of the respective boundaries. In Fig. S4, we show the probability distributions of the bounds $\{\Delta_b^{(3)}, \Delta_b^{(2)}, \Delta_b^{(1)}\}$ for the minimal entanglement parameters $\{\Delta^{\min}, y_c^{\min}\}$ achieved

in the experiment[1].

IV. DATA AND ERROR ANALYSIS

The calibration errors in Table I and the finite quantum efficiencies η_d for the non-number resolving (threshold) detectors D_i may cause the actual entanglement parameters $\{\Delta, y_c\}$ of the physical states $\{\hat{\rho}_W^{(A)}, \hat{\rho}_W^{(\gamma)}\}$, that result from the ideal POVM values of $\{\hat{\Pi}_i^{(c)}, \hat{\Pi}_i^{(s)}\}$, to be inferred incorrectly from our measurements. We describe here how $\{\Delta, y_c\}$ can be conservatively estimated from the photoelectron statistics of the detectors D_i.

First, we confine our analysis to the reduced subspace $\hat{\rho}_r = p_0\hat{\rho}_0 + p_1\hat{\rho}_1 + p_{\geq 2}\hat{\rho}_{\geq 2}$ of the physical density matrices $\{\hat{\rho}_W^{(A)}, \hat{\rho}_W^{(\gamma)}\}$ up to one excitation per mode and ensemble. Importantly, this truncation process can be simulated by local filters on the individual modes of $\{\hat{\rho}_W^{(A)}, \hat{\rho}_W^{(\gamma)}\}$ and leads to a *model-independent inference* of the lower-bound entanglement of the full physical state $\{\hat{\rho}_W^{(A)}, \hat{\rho}_W^{(\gamma)}\}$ (ref.[2,6]). The truncations of $\{\hat{\rho}_W^{(A)}, \hat{\rho}_W^{(\gamma)}\}$ into $\hat{\rho}_r$ also justify the use of single-photon avalanche photodetectors for the (local) y_c-measurement, since threshold detectors with finite efficiencies can be simulated by local filters[2,6]. We extract the photon statistics for the diagonal elements $\{p_0, p_1, p_{\geq 2}\}$ of $\hat{\rho}_r$ by a Bernoulli inversion[7] of the photoelectron statistics at D_i to the photon statistics q_{ijkl} at the faces of the ensembles (ref.[5]). The spin-wave statistics can then be deduced by back-propagating the field statistics at the face of the ensembles to the spin-wave statistics $\{\tilde{p}_0, \tilde{p}_1, \tilde{p}_{\geq 2}\}$ for the reduced subspace of the ensembles, assuming linear mapping from matter to light[8,9].

For the sum uncertainty Δ, we additionally employ a numerical algorithm that estimates the upper bound of Δ for the one-excitation subspace $\hat{\rho}_1$. By defining the success probability $q_i^{(s)}$ for a single-photoelectric detection event $\overline{p}_i$ to arise from $\hat{\rho}_1$, the single-photoelectron probability $\overline{p}_i$ is given by (ref.[4]),

$$\overline{p}_i = q_i^{(s)} p_i^{(s)} + (1 - q_i^{(s)}) p_i^{(f)}. \qquad (1)$$

Here, $p_i^{(s)} = \mathrm{Tr}(\hat{\pi}_i^{(c)}\hat{\rho}_1)$ is the conditional probability for one photon at D_i originating from $\hat{\rho}_1$, normalized with $\sum_i p_i^{(s)} = 1$. On the other hand, $p_i^{(f)}$ is the normalized probability for a false single-photon event based on a spurious detection of a single photoelectron. Such an event can occur with a failure probability $1 - q_i^{(s)}$ if multiple photons are transmitted and registered at the same detector as a single photoelectron, or if the higher order terms $\hat{\rho}_{\geq 2}$ at the faces of the ensembles are transformed into a single photon before the detectors by the lossy propagations (Table I). Eq. 38 of ref.[4] provides the explicit expression for $q_i^{(s)}$. We do not subtract spurious backgrounds from atomic fluorescence, scattering noise, and detector dark counts.

Then, our goal is to unambiguously determine an upper bound of $\Delta = 1 - \sum_i (p_i^{(s)})^2$ for all possible realizations of $p_i^{(f)}$. We constrain this optimization problem with a set of data for the measured single-photoelectron probabilities $\overline{p}_i$ (Δ-measurement) and the photon statistics y_c (thereby, $\{p_0, p_1, p_{\geq 2}\}$ of $\hat{\rho}_r$), as well as the transmission efficiencies in Table I and the detection efficiencies for D_i. With these parameters, we assign the success probability $q_i^{(s)}$ of projecting

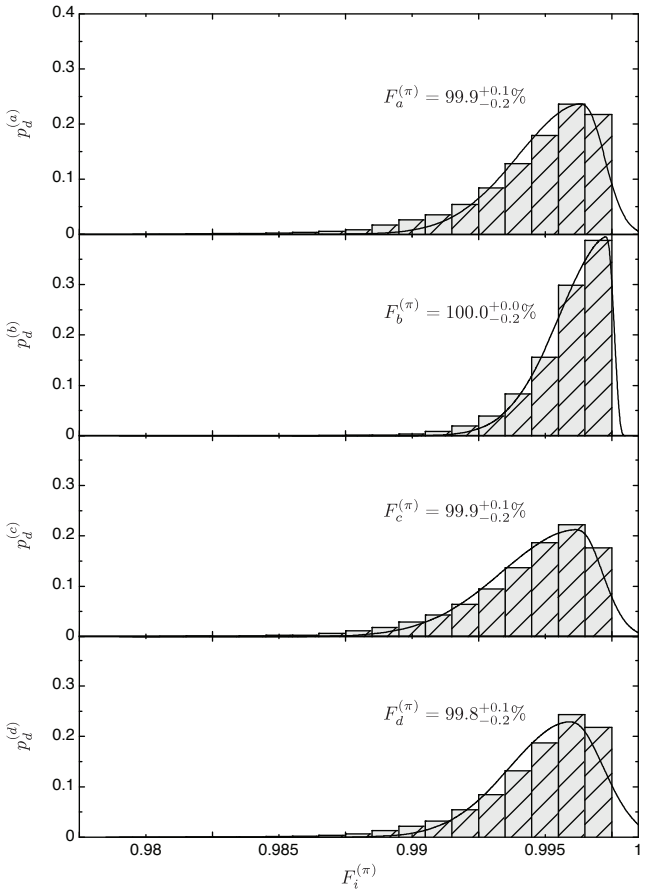

FIG. S3 **Projection fidelities for quantum uncertainty relations.** We show histograms for the projection fidelities $F_i^{(\pi)}$ of the modified operator $\hat{\pi}_i^{(c)}$ to the ideal $\hat{\Pi}_i^{(c)}$ associated with detector D_i for $i \in \{a, b, c, d\}$. The mean value of the projection fidelities of $99.9^{+0.1}_{-0.2}$ % is deduced by fitting the respective probability densities $p_d^{(i)}$ with asymmetric Gaussian distributions $G(F_i^{(\pi)})$ (see the main text).

TABLE I **Experimental imperfections in verification interferometer.** Measured beamsplitter values $\{\alpha, \alpha'\}$ and transmission efficiencies $\{\eta, \eta'\}$ for the verification interferometer in Fig. S2 are shown. The systematic uncertainties $(\delta\kappa)$ of $\{\kappa\}$ are fractionally $(\delta\kappa/\kappa) = 0.05$ for $\kappa \in \{\alpha, \alpha', \eta, \eta'\}$. Note that $\alpha_{12} \simeq \alpha_{34} \simeq \alpha'_{14} \simeq \alpha'_{23} \simeq 1/2$, $\eta_1 \simeq \eta_2 \simeq \eta_3 \simeq \eta_4$, and $\eta'_1 \simeq \eta'_2 \simeq \eta'_3 \simeq \eta'_4$.

α_{12}	α_{34}	α'_{23}	α'_{14}	η_1	η_2	η_3	η_4	η'_1	η'_4	η'_2	η'_3
0.51	0.49	0.50	0.48	0.52	0.54	0.52	0.50	0.95	0.96	0.91	0.93

the purported state $\hat{\rho}_r$ onto $\hat{\pi}_i^{(c)}$. Instead of algebraically upper bounding Δ (ref.[4]), which can yield an unphysically large result $\Delta > 0.75$, we perform a Monte-Carlo analysis to numerically determine a set of $p_i^{(s)}$ that maximizes Δ within the physical limit $\sum_i p_i^{(f)} = 1$ over the distributions of $q_i^{(s)}$. Here, the errors of $q_i^{(s)}$ occur from the systematic uncertainties of $\{\eta, \eta'\}$ and of the detection efficiencies, as well as of the statistical uncertainties of y_c of $\hat{\rho}_r$.

This procedure was employed for all the data sets of Figs. 2 and 3 in the experiment[1] (as well as of Figs. S5 - S7) to obtain conservative estimates of the entanglement parameters $\{\Delta, y_c\}$. The numerical errors for the Monte-Carlo simulations of all the data and the boundaries are well within $< 0.1\%$ of their overall uncertainties. In Fig. S4, we display a histogram for the minimal entanglement parameters $\{\Delta^{\min}, y_c^{\min}\} = \{0.07^{+0.01}_{-0.02}, 0.038 \pm 0.006\}$ (ref.[1]). We find that $\Delta^{\min}$ (black bars) is suppressed below $\Delta_b^{(3)} = 0.261^{+0.010}_{-0.015}$ (red bars) by 10 s.d. We emphasize that we do not subtract any noise in the detection statistics nor do we post-select our data in the analysis, and thereby characterize the quantum state $\{\hat{\rho}_W^{(A)}, \hat{\rho}_W^{(\gamma)}\}$ that is physically available to the user.

V. THEORETICAL MODEL FOR THE QUANTUM INTERFACE

We describe theoretical models for the generation, storage, and transfer of the multipartite atomic state $\hat{\rho}_W^{(A)} = \mathrm{Tr}_h(\hat{\Pi}_h \hat{U}^\dagger_{\mathrm{write}} \hat{\rho}_g^{(A)} \hat{U}_{\mathrm{write}})$ to the photonic state of $\hat{\rho}_W^{(\gamma)} = \mathrm{Tr}_A(\hat{U}^\dagger_{\mathrm{read}} \hat{\rho}_W^{(A)} \hat{U}_{\mathrm{read}})$.

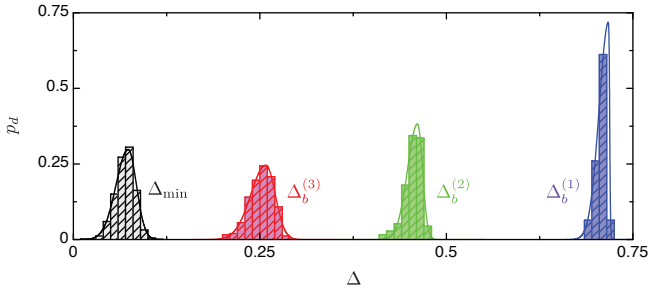

FIG. S4 **Numerical optimizations for the minimal entanglement parameters and the uncertainty bounds.** Histograms of a Monte-Carlo analysis for minimizing 1-mode bound $\Delta_b^{(1)}$ (purple bars), 2-mode bound $\Delta_b^{(2)}$ (green bars), and 3-mode bound $\Delta_b^{(3)}$ (red bars) are shown for the smallest measured values of the entanglement parameters $\{\Delta^{\min}, y_c^{\min}\}$ (black bars) in ref.[1]. The vertical axis is the probability density p_d corresponding to the respective value of Δ. The lines are fits to Gaussian distributions $p_d(\Delta) = G(\Delta)$ with asymmetric widths for ± 1 s.d.

A. Entanglement generation

First, we begin our model with an interaction Hamiltonian (ref.[10])

$$\hat{H}^{(\epsilon)}_{\mathrm{write}}/\hbar = \frac{g_0 \Omega^{(\epsilon)}_{\mathrm{write}}}{\delta} (\hat{a}_{\gamma_1} \hat{S}_\epsilon + \hat{a}^\dagger_{\gamma_1} \hat{S}^\dagger_\epsilon) \tag{2}$$

for the parametric writing process of ensemble ϵ with excitation parameter $\xi = \tanh(g_0 \Omega^{(\epsilon)}_{\mathrm{write}} \Delta t_w / \delta)$. Here, $\Omega^{(\epsilon)}_{\mathrm{write}}$ (δ) is the Rabi frequency (detuning) of the writing laser, and $\hat{a}_{\gamma_1}$ ($\hat{S}_\epsilon$) is the annihilation operator for the fields γ_1 (collective excitations in ensemble ϵ). The writing process transforms the initial atomic state $|\overline{g}_\epsilon\rangle$ into individual products of two-mode squeezed states between the fields γ_1 and ensembles ϵ via $\hat{U}_{\mathrm{write}} = \prod_\epsilon \exp(i \Delta t_w \hat{H}^{(\epsilon)}_{\mathrm{write}}/\hbar)$, with the writing phases $\{\phi_1^{(w)}, \phi_2^{(w)}, \phi_3^{(w)}\}$ included in $\Omega^{(\epsilon)}_{\mathrm{write}}$.

Upon the transformation of the fields γ_1 by our heralding interferometer, we find that the output mode operator for γ_1 is given by (up to an overall normalization) $\hat{a}_h \mapsto \hat{a}_{a_1} + e^{i\phi_1^{(h)}} \hat{a}_{b_1} + e^{i\phi_2^{(h)}} (\hat{a}_{c_1} + e^{i\phi_3^{(h)}} \hat{a}_{d_1})$, where $\hat{a}_{i_1}$ is the mode operator for the field $i_1 \in \gamma_1$. Here, we omit the vacuum terms because we make use of normally ordered expectation values. Additionally, the heralding measurement $\hat{\Pi}_h$ with the threshold detector D_h is modeled with η_h, describing the overall efficiency for detecting γ_1 (including losses in the heralding channels, quantum efficiency of D_h and mode-matching efficiency to the collective state[11]), where

$$\hat{\Pi}_h = 1 - \sum_{n=0}^{\infty} \frac{:(-\eta_h \hat{a}^\dagger_h \hat{a}_h)^n:}{n!}. \tag{3}$$

Therefore, by calculating $\hat{\rho}_W^{(A)} = \mathrm{Tr}_h(\hat{\Pi}_h \hat{U}^\dagger_{\mathrm{write}} \hat{\rho}_g^{(A)} \hat{U}_{\mathrm{write}})$ for $\hat{\rho}_g^{(A)} = |\overline{g}_\epsilon\rangle\langle\overline{g}_\epsilon|$ and $\eta_h \ll 1$, we obtain the analytic expression of the atomic state $\hat{\rho}_W^{(A)}$ in Eq. 3 of ref.[1] with the ideal case without additional noise (see section V.D for our noise model). The atomic entangled state $\hat{\rho}_W^{(A)}$ is thereby obtained non-destructively from a quantum measurement $\hat{\Pi}_h$ on the heralding systems γ_1, whereby the higher order contamination $\hat{\rho}^{(A)}_{\geq 2}$ scales with ξ instead of ξ^2. The creation of $\hat{\rho}_W^{(A)}$ is then heralded by the photoelectric detection $\hat{\Pi}_h$ of the fields γ_1 with probability $p_h = \mathrm{Tr}(\hat{\Pi}_h \hat{U}^\dagger_{\mathrm{write}} \hat{\rho}_g^{(A)} \hat{U}_{\mathrm{write}})$.

B. Entanglement transfer

The transfer of the stored quadripartite entanglement to the photonic entanglement is described by a linear mapping process $\hat{U}_{\mathrm{read}}$ (ref.[12]), which transfers the delocalized collective state $|\overline{s}_\epsilon\rangle$ of the ensembles ϵ to the individual fields γ_2 with retrieval efficiency η_{read}. The reading process then generates a photonic state $\hat{\rho}_W^{(\gamma)} = \mathrm{Tr}_A(\hat{U}^\dagger_{\mathrm{read}} \hat{\rho}_W^{(A)} \hat{U}_{\mathrm{read}})$ via a 'beamsplitter' rotation $\hat{U}_{\mathrm{read}}$ of $\hat{\rho}_W^{(A)}$ into $\hat{\rho}_W^{(\gamma)}$ with a ratio given by η_{read} (and reading phases

$\{\phi_1^{(r)}, \phi_2^{(r)}, \phi_3^{(r)}\}$), after which the atomic states are traced over.

C. Entanglement verification

Finally, we model the photoelectric detection statistics of the photonic state $\hat{\rho}_W^{(\gamma)}$ at $D_{a,b,c,d}$. The detection probabilities for the output channels $\gamma_2' = \{a_2', b_2', c_2', d_2'\}$ of the entanglement verification setups in Figs. S1b and S2 can be modeled with projectors

$$\hat{\Pi}_0^{(\gamma_2')} = \sum_{n=0}^{\infty} \frac{:(-\eta_{\gamma_2'} \hat{a}_{\gamma_2'}^{\dagger} \hat{a}_{\gamma_2'})^n:}{n!} \tag{4}$$

for null events, and

$$\hat{\Pi}_1^{(\gamma_2')} = 1 - \hat{\Pi}_0^{(\gamma_2')} \tag{5}$$

for events that register one or more photons. Here, $\eta_{\gamma_2'}$ is the overall efficiency for detecting a photon in field γ_2' at $D_{a,b,c,d}$.

The photoelectric detection probabilities $\overline{p}_{ijkl}^{(c,s)}$ for counting i,j,k,l photoelectrons at $D_{a,b,c,d}$ can be calculated from the projectors $\hat{\Pi}_{ijkl}^{(c,s)} = \hat{\Pi}_i^{(a_2')} \hat{\Pi}_j^{(b_2')} \hat{\Pi}_k^{(c_2')} \hat{\Pi}_l^{(d_2')}$, via $\overline{p}_{ijkl}^{(c,s)} = \mathrm{Tr}(\hat{\Pi}_{ijkl}^{(c,s)} \hat{\rho}_W^{(\gamma)})$, for the respective configurations $\{c,s\}$ of Δ and y_c setups in Fig. S1b. Finally, the mode operator $\hat{a}_{\gamma_2'}$ for the output channel γ_2' is given by $(\hat{a}_{a_2'}, \hat{a}_{b_2'}, \hat{a}_{c_2'}, \hat{a}_{d_2'})^T = \hat{U}^{(c,s)} \cdot (\hat{a}_{a_2}, \hat{a}_{b_2}, \hat{a}_{c_2}, \hat{a}_{d_2})^T$. Here, the transfer matrix $\hat{U}^{(c,s)}$ is (i) a unity matrix $\hat{U}^{(s)} = \mathbf{I}$ for the y_c-measurement, and (ii)

$$\hat{U}^{(c)} = \frac{1}{2} \begin{pmatrix} 1 & e^{i\beta_1} & e^{i\beta_2} & e^{i(\beta_2+\beta_3)} \\ 1 & -e^{i\beta_1} & -e^{i\beta_2} & e^{i(\beta_2+\beta_3)} \\ 1 & -e^{i\beta_1} & e^{i\beta_2} & -e^{i(\beta_2+\beta_3)} \\ 1 & e^{i\beta_1} & -e^{i\beta_2} & -e^{i(\beta_2+\beta_3)} \end{pmatrix} \tag{6}$$

for the Δ-measurement (Fig. S2), where we assume balanced loss in writing Eq. 6, but not for our general analysis.

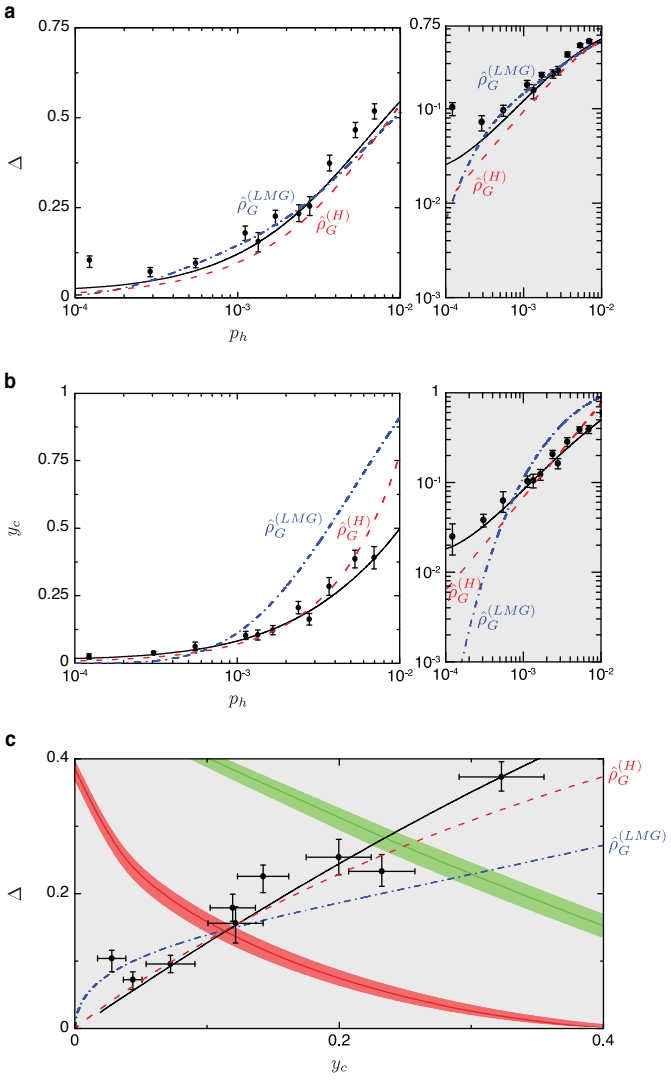

FIG. S5 **Statistical evolutions of the individual entanglement parameters.** The data points and black line depict the statistical dependences of **a,** Δ and **b,** y_c to the heralding probability $p_h(\xi)$ for Fig. 2b in ref.[1]. **c,** We also display the expanded view of the entanglement parameters $\{\Delta, y_c\}$ depicting the statistical transitions of multipartite atomic entanglement (inset of Fig. 2b in ref.[1]). The thermal behaviors $\{\Delta^{(T)}, y_c^{(T)}\}$ of the thermal equilibrium states $\hat{\rho}_G^{(\mathrm{H})}$ and $\hat{\rho}_G^{(\mathrm{LMG})}$ of the Heisenberg-like and the Lipkin-Meshkov-Glick models are shown as red dashed and blue dash-dotted lines, respectively. Here, the horizontal axis is the heralding probability $p_h(\xi)$, with thermal excitation given by $\xi = e^{-\beta_T J}$ for the spin models.

D. Incorporating noise into the model

To include the effects of atomic fluorescence and laser scattering noise emanating from the writing and reading processes, as well as of the background contamination including dark counts in the detectors, we mix dephased coherent states $\hat{\rho}_{r_B,q} = \int ||r_B|e^{i\phi_q}\rangle_q \langle |r_B|e^{i\phi_q}| d\phi_q$ and $\hat{\rho}_{r_I,q} = \int ||r_I|e^{i\phi_q}\rangle_q \langle |r_I|e^{i\phi_q}| d\phi_q$ into quantum channels $q \in \{\gamma_1, \gamma_2\}$ of the initial state, and find that

$$\hat{\rho}_g^{(A)} = \prod_{\epsilon} |\overline{g}_\epsilon\rangle\langle\overline{g}_\epsilon| \prod_{\gamma_1} (\hat{\rho}_{r_B,\gamma_1} \otimes \hat{\rho}_{r_I,\gamma_1}) \prod_{\gamma_2} (\hat{\rho}_{r_B,\gamma_2} \otimes \hat{\rho}_{r_I,\gamma_2}), \tag{7}$$

with quantum fields $\gamma_1 = \{a_1, b_1, c_1, d_1\}$, $\gamma_2 = \{a_2, b_2, c_2, d_2\}$. Here, $\{r_B, r_I\}$ are the respective probability amplitudes for the background and intensity-dependent noises (atomic fluorescence and scattering noise). In the experiment, we directly measure the noises $|r_{B,\gamma_1}|^2$, $|r_{B,\gamma_2}|^2$ and $|r_{I,\gamma_2}|^2$. We also infer the heralding and retrieval efficiencies $\{\eta_h, \eta_{\mathrm{read}}\}$ (see ref.[1]), as well as the scattering noise $|r_{I,\gamma_1}|^2 \propto |\Omega_{\mathrm{write}}^{(\epsilon)}|^2$ for the writing laser by independently measuring the individual quantum correlation functions g_{γ_1,γ_2} for the fields $\{\gamma_1, \gamma_2\}$, following the methods in refs.[8,9,11].

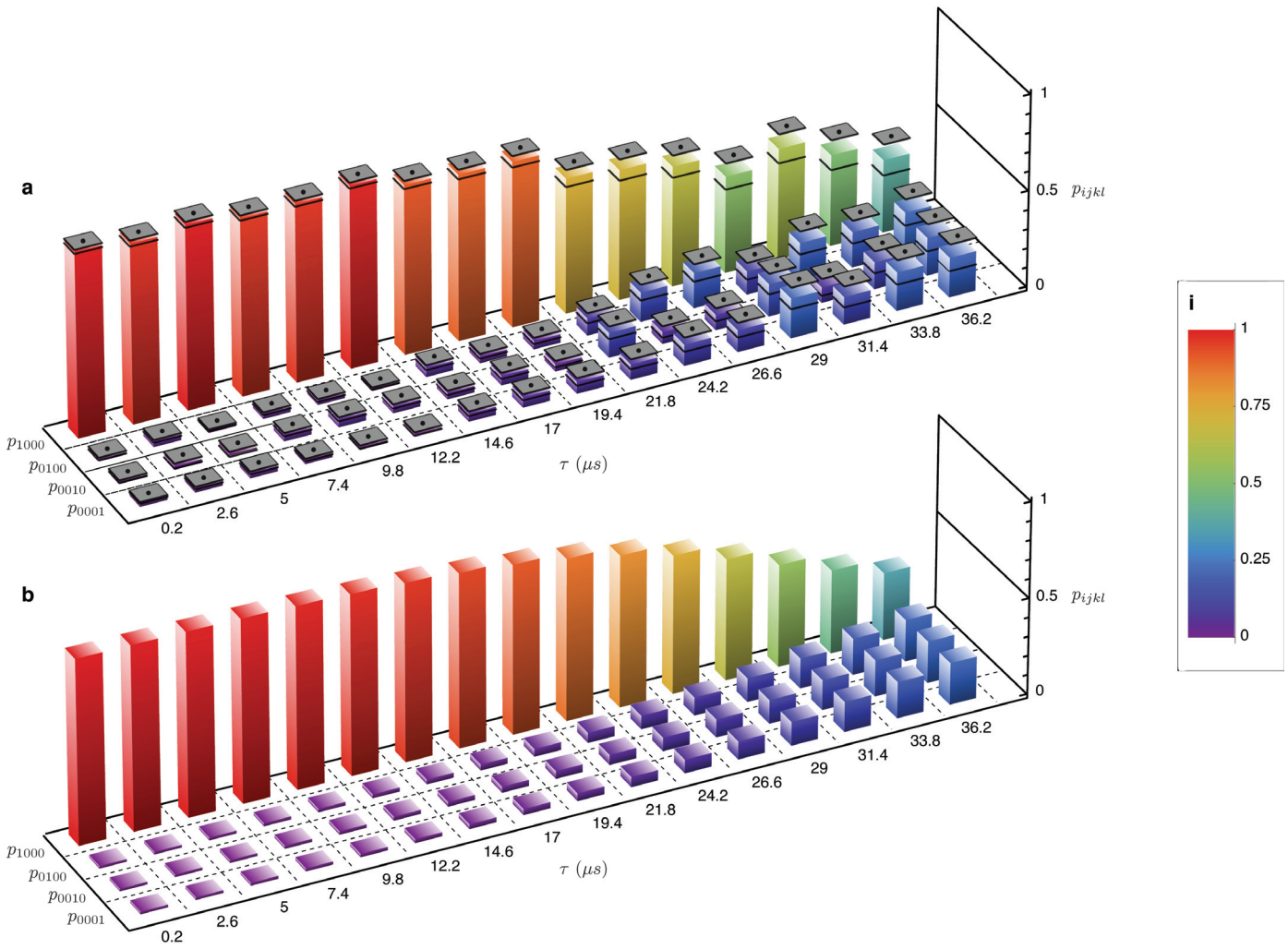

FIG. S6 **Temporal decay of coherences stored in four atomic ensembles. a,** Evolution of the photon probabilities $\{p_{1000}, p_{0100}, p_{0010}, p_{0001}\}$ for occupying the output modes of the verification interferometer (Δ-measurement) versus storage time τ. For readability, the heights of the bars are shown in accord to the color convention of the inset **i**. Error bars, shown as grey squares, reflect the statistical uncertainties for each point. **b,** Photon probabilities $\{p_{1000}, p_{0100}, p_{0010}, p_{0001}\}$ from our theoretical model, which assumes a memory time determined from the temperature of the cold atomic samples and the net momentum transfer to the atomic spin-waves.

Finally, using the initial state of $\hat{\rho}_g^{(A)}$ in Eq. 7, we approximate the physical state of $\hat{\rho}_W^{(A)} = \mathrm{Tr}_h(\hat{\Pi}_h \hat{U}_{\mathrm{write}}^{\dagger} \hat{\rho}_g^{(A)} \hat{U}_{\mathrm{write}})$. We then simulate $\hat{\rho}_W^{(\gamma)} = \mathrm{Tr}_A(\hat{U}_{\mathrm{read}}^{\dagger} \hat{\rho}_W^{(A)} \hat{U}_{\mathrm{read}})$ as well as the various expectation values of $\langle \hat{\Pi}_{ijkl}^{(c,s)} \rangle$ associated with the photoelectron statistics $\overline{p}_{ijkl}^{(c,s)}$ of $\{\Delta, y_c\}$. Finally, we perform the numerical algorithm described in section IV and obtain the theoretical expectations of $\{\Delta_{\mathrm{th}}, (y_c)_{\mathrm{th}}\}$ as functions of heralding probability p_h, shown in Fig. S5. The theoretical curves in the experiment[1] are given by the parametric dependences of the entanglement parameters $\{\Delta_{\mathrm{th}}, (y_c)_{\mathrm{th}}\}$ to the heralding probability p_h.

VI. TEMPORAL DYNAMICS OF ATOMIC MULTIPARTITE ENTANGLEMENT

As described in the Methods, the decoherence mechanism for the atomic W-state $\hat{\rho}_W^{(A)}(\tau)$ is dictated primarily by the motional dephasings of spin-waves[13]. Qualitatively, the dephasings of the ensembles $\epsilon = \{a, b, c, d\}$ arise from independent evolutions of the spatial phases $\phi_j^{(sw)}(\tau) = \delta\vec{k} \cdot \vec{r}_j(\tau) + \phi_i$ imprinted on the spin-waves $|\overline{s}_\epsilon(\tau)\rangle = \sum_j e^{i\phi_j^{(sw)}(\tau)} |g \cdots s_j \cdots g\rangle_\epsilon$ due to thermal motions, where $\delta\vec{k} = \vec{k}_w - \vec{k}_1$ and $\phi_i = \phi_i^{(w)} - \phi_i^{(h)}$. Specifically, by assuming a Boltzmann velocity distribution with a mean velocity v_t for each ensemble ϵ, we find analytically that the probability p_c for the coherent atomic component $\hat{\rho}_c^{(A)}$ of $\hat{\rho}_W^{(A)}(\tau)$ decays over time τ, following $p_c \propto |\langle \overline{s}_\epsilon(0) | \overline{s}_\epsilon(\tau) \rangle|^2 \simeq$

$e^{-\tau^2/\tau_m^2} + \mathcal{O}(1/N_{A,\epsilon})$ (refs.[13,14]).

We follow a procedure similar to section V to simulate the dynamics of the atomic W-state $\hat{\rho}_W^{(A)}(\tau)$. In particular, absent any noise (i.e. $\hat{\rho}_g^{(A)} = |\overline{g}_\epsilon\rangle\langle\overline{g}_\epsilon|$) and for $\eta_h \ll 1$, we obtain the atomic dynamics

$$\hat{\rho}_W^{(A)}(\tau) \simeq (1-3\xi)(\cos^2\theta(\tau)\hat{\rho}_c^{(A)} + \sin^2\theta(\tau)\hat{\rho}_n^{(A)}) + 3\xi\hat{\rho}_{\geq 2}^{(A)} + \mathcal{O}(\xi^2), \quad (8)$$

where the mixing angles are $\cos^2\theta(\tau) = e^{-\tau^2/\tau_m^2}$ and $\sin^2\theta(\tau) = 1 - e^{-\tau^2/\tau_m^2}$. Thus, the decoherence for the atomic W-state results from the incoherent mixing of the initial superradiant state $\hat{\rho}_c^{(A)} \simeq |W\rangle_A\langle W|$ at $\tau = 0$ to mixtures of subradiant states $\hat{\rho}_n^{(A)}$ at $\tau > 0$, which increase the vacuum component $\hat{\rho}_0$ for the photonic state $\hat{\rho}_W^{(\gamma)}$. In turn, the increase of the subradiant states $\hat{\rho}_n^{(A)}$ contributes to a reduction in the coherent component $\hat{\rho}_c^{(A)}$ of $\hat{\rho}_W^{(A)}(\tau)$, as well as to a build-up of uncorrelated atomic noise $\hat{\rho}_{\geq 2}^{(A)}$ relative to $\hat{\rho}_c^{(A)}$. The net effect is a simultaneous degradation of the entanglement parameters $\{\Delta, y_c\}$ with a time-scale $\tau_m = 1/(|\delta\vec{k}|v_t) \simeq 17\ \mu s$. For the actual simulations in ref.[1], we perform the full calculations including section V to incorporate the atomic fluorescence, laser scattering and background noise.

Fig. S6 illustrates the temporal reduction in the overall coherence $\overline{d}$ of the full quadripartite state in our experiment[1]. Operationally, the loss of coherence is observed in terms of the decrease in imbalances among $\{p_{1000}, p_{0100}, p_{0010}, p_{0001}\}$ as a function of storage time τ, and hence to an increase in Δ. The behavior of the experimentally observed photon probabilities in Fig. S6a results from the progressive decay of the initial coherence for $\hat{\rho}_W^{(A)}(\tau_0)$ at $\tau_0 = 0.2\ \mu s$ for which $V_{\text{eff}}(\tau_0) = 4\overline{d} = 0.95 \pm 0.02$, evolving then to $V_{\text{eff}}(\tau_f) = 0.10^{+0.25}_{-0.10}$ for the final state $\hat{\rho}_W^{(A)}(\tau_f)$ measured at $\tau_f = 36.2\ \mu$s. The observed evolution is qualitatively in good agreement with our theoretical model of the photon probabilities shown in Fig. S6b. The spin-wave statistics are similarly modified by phase decoherence leading to an increase of y_c, from $y_c(\tau_0) = 0.03 \pm 0.01$ to $y_c(\tau_f) = 0.74 \pm 0.34$.

Finally, in Fig. S7, we show the dissipative dynamics of the atomic W-state[1], displayed independently for $\Delta(\tau)$ (Fig. S7a) and $y_c(\tau)$ (Fig. S7b). The complete 3-dimensional dynamics of the atomic W-states is displayed in Fig. 3 of ref.[1] (See also the Supplementary Movie). The temporal behaviors of $\{\Delta(\tau), y_c(\tau)\}$ in our experiment[1] of the quadripartite atomic state (black points) are in qualitatively good agreement with the simulated dynamics for $\hat{\rho}_W^{(A)}(\tau)$ (black line). However, for Δ, we find that our data points consistently lie above the theoretical dynamics for $\hat{\rho}_W^{(A)}(\tau)$.

One possible explanation is that for the Δ-measurement, stringent interferometric stabilities and excellent overlaps $\overline{\lambda}$, close to unity, are required for all the 16 spatio-temporal modes $\{\vec{k}, s\}$, composed of the 8 quantum fields $\gamma_1 = \{a_1, b_1, c_1, d_1\}$ and $\gamma_2 = \{a_2, b_2, c_2, d_2\}$, as well as of the 8 classical writing and reading pulses, with s corresponding to the polarization state of each field. Ultimately, the wavepacket overlap for the entangled fields $\gamma_2 = \{a_2, b_2, c_2, d_2\}$ is limited by the differential optical depths of the cold samples $\{a, b, c, d\}$, which in turn yield differential group velocities during the slow light process of coherent transfer from $\hat{\rho}_W^{(A)}$ to $\hat{\rho}_W^{(\gamma)}$ by way of dynamic electromagnetically induced transparency[12].

We include this effect in the model via a field overlap $\overline{\lambda}$ (ref.[15]), where a fit corresponding to Fig. S5 gives $\overline{\lambda} = 0.98$ ($\overline{\lambda} = 0.95$ for Fig. S7a), with similar results obtained from the calculation of overlap for the measured temporal shapes of

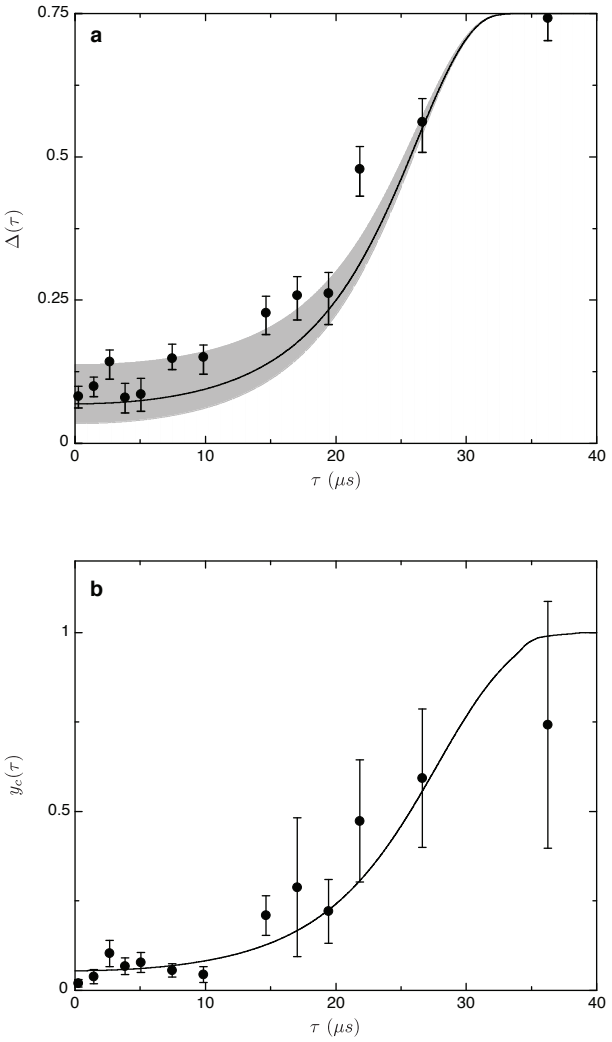

FIG. S7 **Temporal evolutions of the individual entanglement parameters.** Due to the motional dephasings of the spin-waves, the experimentally measured entanglement parameters (black points), for **a,** $\Delta(\tau)$, and for **b,** $y_c(\tau)$, increase with a time-scale $\tau_m \simeq 17\mu s$. The theoretical simulation for the temporal behavior of $\{\Delta, y_c\}$ is displayed as a black solid line. The gray band around the theoretical curve $\delta(\tau)$ represents the $1/e$ uncertainty of the simulation due to the systematic error of the measured overlap $\overline{\lambda}$.

the wave-packets $\gamma_2 = \{a_2, b_2, c_2, d_2\}$. For the simulated dynamics of Fig. 3a in ref.[1], we use the field overlaps $\overline{\lambda}$ obtained independently from classical measurements of the interferometric visibility for both 'classical' (write, read) and 'quantum' interferometers (quantum fields γ_1, γ_2). Thus, the discrepancy in $\Delta(\tau)$ can be largely attributed to the systematic uncertainty in the inference of $\overline{\lambda} = 0.97 \pm 0.03$, with the uncertainty corresponding to the dynamics of $\Delta(\tau)$ shown as a gray band in Fig. S7a.

VII. ENTANGLEMENT THERMALIZATION

Here, we formulate the thermal equilibrium state $\hat{\rho}_G$ (refs.[16,17]) of a Heisenberg-like model $\hat{H}_{\rm H}$ and a Lipkin-Meshkov-Glick model $\hat{H}_{\rm LMG}$, as presented in Fig. 2b of ref.[1] (see also Fig. S5c). We compare the entanglement parameters $\{\Delta^{(T)}, y_c^{(T)}\}$ obtained from $\hat{H}_{\rm H}$ and $\hat{H}_{\rm LMG}$ to the observed statistical behavior of the quadripartite states of the ensembles in ref.[1].

A. Heisenberg-like model

We begin with a Heisenberg-like Hamiltonian $\hat{H}_{\rm H}$ of four ($N_s = 4$) spins $\{i, j\}$ of spin vectors $\vec{S}^{(i)} = \{\hat{S}_x^{(i)}, \hat{S}_y^{(i)}, \hat{S}_z^{(i)}\}$ with isotropic infinite-ranged ferromagnetic interaction ($J_{ij} = J > 0$ for all $\{i, j\}$), where

$$\hat{H}_{\rm H} = -\frac{J}{N_s} \sum_{\langle i,j \rangle} \vec{S}^{(i)} \cdot \vec{S}^{(j)} + h_z \sum_i \hat{S}_z^{(i)} + \hat{H}_p.$$

Here, $\hat{H}_{\rm H}$ includes a standard Heisenberg interaction $-\frac{J}{N_s} \sum_{\langle i,j \rangle} \vec{S}^{(i)} \cdot \vec{S}^{(j)} + h_z \sum_i \hat{S}_z^{(i)}$, as well as a spin-projection term $\hat{H}_p = 2h_z |S, -S\rangle\langle S, -S|$ which selects out the collective spin state $|S, -S\rangle$ with bias energy $2h_z$ and suppresses the thermal equilibrium population of $|S, -S\rangle$.

Since the Hamiltonian $\hat{H}_{\rm H}$ commutes with the collective spin operators $\{\vec{S}^2, \hat{S}_z\} \equiv \{(\sum_i \vec{S}^{(i)})^2, \sum_i \hat{S}_z^{(i)}\}$, $\hat{H}_{\rm H}$ is diagonal in the basis of collective spin states $|S, M\rangle$ for $0 \leq S \leq N_s/2$ and $-S \leq M \leq S$. The eigenenergies are

$$\mathcal{E}_{S,M} = \begin{cases} -\frac{J}{4} S(S+1) + h_z M + \frac{3J}{4}, & \text{if } |S, M\rangle \neq |2, -2\rangle \\ -\frac{3J}{4}, & \text{if } |S, M\rangle = |2, -2\rangle. \end{cases}$$

The degeneracy for $|S, M\rangle$ is given by $D_S = \frac{(2S+1)N_s!}{(N_s/2+S+1)!(N_s/2-S)!}$ (ref.[7]). Importantly, for any value of $h_z > 0$, the ground state is $|2, -1\rangle \equiv |W_1\rangle = \frac{1}{2}(|1000\rangle + |0100\rangle + |0010\rangle + |0001\rangle)$ with energy $\mathcal{E}_{2,-1} = -\frac{3J}{4} - h_z$. In the following sections, we will set the magnetic field to $h_z = J/2$.

B. Thermal equilibrium state

We solve for the Gibbs state, $\hat{\rho}_G^{(\rm H)} = \frac{1}{Z} e^{-\beta_T \hat{H}_{\rm H}}$, where $Z = {\rm Tr}(e^{-\beta_T \hat{H}_{\rm H}})$ is the partition function and beta parameter $\beta_T = 1/k_B T$ for thermal energy $k_B T$ at temperature T. Explicitly, we obtain $\hat{\rho}_G^{(\rm H)} = \frac{1}{Z} \sum_{S,M} D_S e^{-\beta_T \mathcal{E}_{S,M}} \hat{\rho}_{S,M}$. Here, the component $\hat{\rho}_{S,M}$ is a mixed state that contains all possible $|S, M\rangle$ for the degeneracy of D_S; e.g., $\hat{\rho}_{1,-1} = \frac{1}{3}(|W_2\rangle\langle W_2| + |W_3\rangle\langle W_3| + |W_4\rangle\langle W_4|)$ is a mixture of three non-symmetrized single-excitation W-states, $\{|W_2\rangle, |W_3\rangle, |W_4\rangle\}$.

By mapping the spin-states to number-states ($|\downarrow, \uparrow\rangle \mapsto$

$|0,1\rangle)$[18], we obtain a Gibbs number-state $\hat{\rho}_G^{(n)}$ in the form of

$$\hat{\rho}_G^{(n)}(T) = p_0\hat{\rho}_0 + p_1\hat{\rho}_1 + p_{\geq 2}\hat{\rho}_{\geq 2}, \tag{9}$$

as in the reduced density matrices $\hat{\rho}_r$ of $\{\hat{\rho}_W^{(A)}, \hat{\rho}_W^{(\gamma)}\}$. Our goal is to calculate the thermal (T) behavior of multipartite entanglement[16,17] for $\hat{\rho}_G^{(n)}$ via the entanglement parameters $\{\Delta^{(T)}, y_c^{(T)}\}$.

Because the vacuum component $\hat{\rho}_0$ and the higher order terms $\hat{\rho}_{\geq 2}$, as well as the non-symmetric single-excitation states $\hat{\rho}_{1,-1}$ of $\hat{\rho}_1$ are more energetic than the ground state $|W_1\rangle$, the Gibbs state $\hat{\rho}_G^{(n)}(T=0)$ is the symmetric W-state $|W_1\rangle\langle W_1|$ at zero temperature. For low temperature ($\beta_T \gg 1$), we approximate $\hat{\rho}_G^{(n)}$ by

$$\hat{\rho}_G^{(n)}(T) \simeq \frac{1}{Z}(Z_0\hat{\rho}_0 + Z_1\hat{\rho}_1 + (1 - Z_1 - Z_0)\hat{\rho}_{\geq 2}), \tag{10}$$

with $Z_0 = e^{\frac{3\beta_T J}{4}}$ and $Z_1 = Z_W + 3Z_X$. The single-excitation subspace $\hat{\rho}_1$ is

$$\hat{\rho}_1(T) \simeq \frac{1}{Z_1}(Z_W|W_1\rangle\langle W_1| + 3Z_X\hat{\rho}_{1,-1}), \tag{11}$$

with $Z_W = e^{\frac{\beta_T(4h_z+3J)}{4}}$, $Z_X = e^{\frac{\beta_T(4h_z-J)}{4}}$. Here, the thermal excitations from the ground state $|W_1\rangle\langle W_1|$ to one of $\hat{\rho}_{1,-1}$ occur with probability $\xi = Z_X/Z_W = e^{-\beta_T J}$.

C. Entanglement parameters

For the sum uncertainty $\Delta^{(T)}$, we only consider the single-excitation subspace $\hat{\rho}_1$ (Eq. 11). The probability to find $|W_1\rangle$ is $p_{1000} = \langle W_1|\hat{\rho}_1|W_1\rangle = \frac{1}{1+3e^{-\beta_T J}}$, whereas the probabilities to find the non-symmetric states are $p_{0100} = p_{0010} = p_{0001} = \frac{e^{-\beta_T J}}{1+3e^{-\beta_T J}}$. For $\beta_T \gg 1$, we deduce the sum uncertainty $\Delta^{(T)} \simeq 6e^{-\beta_T J} = 6\xi$. Similarly, we find the quantum statistics $y_c^{(T)} \simeq \frac{16}{3}e^{-\beta_T J} = \frac{16}{3}\xi$. Thus, the parametric relation

$$\Delta^{(T)} \simeq 6 \times \frac{3}{16}y_c^{(T)} = \frac{9}{8}y_c^{(T)} \tag{12}$$

replicates the statistical behavior of $\Delta_{\text{th}} \simeq \frac{9}{8}(y_c)_{\text{th}}$ for the ensembles (section V) in the low-excitation regime (equivalent to $\beta_T \gg 1$).

By performing the full calculation of $\{\Delta^{(T)}, y_c^{(T)}\}$ for $\hat{\rho}_G^{(n)}$ without any approximations and by inserting the excitation probability $\xi = e^{-\beta_T J}$ into the expression of heralding probability $p_h(\xi)$ for $\hat{\rho}_W^{(A)}$ (section V), we compare the theoretical expectations $\{\Delta^{(T)}, y_c^{(T)}\}$ of the thermal state $\hat{\rho}_G^{(\text{H})}$ to the experimental data, presented in Fig. 2b as a red dashed line (ref.[1]; see also Fig. S5c). In Fig. S5, we plot the dependences of the individual parameters $\Delta^{(T)}$ and $y_c^{(T)}$ to p_h as red dashed lines. The panels on the right-hand side show the log-log scale plots of the figures for small values of ξ.

D. Lipkin-Meshkov-Glick model

We simulate the entanglement parameters $\{\Delta^{(T)}, y_c^{(T)}\}$ of a thermal equilibrium state $\hat{\rho}_G^{(\text{LMG})}$ for an isotropic Lipkin-Meshkov-Glick (LMG) Hamiltonian $\hat{H}_{\text{LMG}}$ (ref.[19]), where

$$\hat{H}_{\text{LMG}} = -\frac{J}{4}\sum_{\langle i,j\rangle}(\hat{S}_x^{(i)}\hat{S}_x^{(j)} + \hat{S}_y^{(i)}\hat{S}_y^{(j)}) + h_z\sum_i \hat{S}_z^{(i)},$$

with infinite-range interactions $J > 0$. The energy states are the collective spin states $|S, M\rangle$ with the eigenenergy $\mathcal{E}_{S,M} = -\frac{J}{4}(S(S+1) - M^2) + \frac{J}{2} + h_z M$. By setting $h_z = J/2$, the ground state can be made $|W_1\rangle$. Proceeding with the methods in sections VII.B-VII.C, we calculate $\{\Delta^{(T)}, y_c^{(T)}\}$ for the Gibbs state $\hat{\rho}_G^{(\text{LMG})}$ of $\hat{H}_{\text{LMG}}$, as depicted in the blue dash-dotted lines of Fig. S5 and Fig. 2b of ref.[1].

References

1. Choi, K. S., Goban, A., Papp, S. B., van Enk, S. J & Kimble, H. J. Entanglement of spin waves among four quantum memories. *Nature* (2010).
2. van Enk, S. J., Lütkenhaus, N. & Kimble, H. J. Experimental procedures for entanglement verification. *Phys. Rev. A* **75**, 052318 (2007).
3. Balić, V., Braje, D. A., Kolchin, P., Yin, G. Y. & Harris, S. E. Generation of paired photons with controllable waveforms. *Phys. Rev. Lett.* **94**, 183601 (2005).
4. Lougovski, P. *et al.* Verifying multipartite mode entanglement of W states. *New J. Phys.* **11**, 063029 (2009).
5. Papp, S. B. *et al.* Characterization of multipartite entanglement for one photon shared among four optical modes. *Science* **324**, 764-768 (2009).
6. Chou, C. W. *et al.* Measurement-induced entanglement for excitation stored in remote atomic ensembles. *Nature* **438**, 828-832 (2005).
7. Mandel, L. & Wolf, E. *Optical Coherence and Quantum Optics* (Cambridge University Press, Cambridge, 1995).
8. Laurat, J., Choi, K. S., Deng, H., Chou, C. W. & Kimble, H. J. Heralded entanglement between atomic ensembles: Preparation, decoherence, and scaling. *Phys. Rev. Lett.* **99**, 180504 (2007).
9. Choi, K. S., Deng, H., Laurat, J. & Kimble, H. J. Mapping photonic entanglement into and out of a quantum memory. *Nature* **452**, 67-71 (2008).
10. Duan, L.-M., Lukin, M. D., Cirac, J. I. & Zoller, P. Long-distance quantum communication with atomic ensembles and linear optics. *Nature* **414**, 413-418 (2001).
11. Chou, C. W., Polyakov, S. V., Kuzmich, A. & Kimble, H. J. Single-photon generation from stored excitation in an atomic ensemble. *Phys. Rev. Lett.* **92**, 213601 (2004).
12. Fleischhauer, M. & Lukin, M. D. Dark-state polaritons in electromagnetically induced transparency. *Phys. Rev. Lett.* **84**, 5094-5097 (2000).
13. Simon, J., Tanji, H. Thompson, J. K. & Vuletić, V. Interfacing collective atomic excitations and single photons. *Phys. Rev. Lett.* **98**, 183601 (2007).
14. Zhao, B. *et al.* A millisecond quantum memory for scalable quantum networks. *Nature Phys.* **5**, 95-99 (2009).
15. Legero, T., Wilk, T., Kuhn, A. & Rempe, G. Time-resolved two-photon quantum interference. *Appl. Phys. B* **77**, 797-802 (2003).
16. Gühne, O. & Tóth, G. Energy and multipartite entanglement in multi-dimensional and frustrated spin models. *Phys. Rev. A* **73**, 052319 (2006).
17. Amico, L., Fazio, R., Osterloh, A. & Vedral, V. Entanglement in many-body systems. *Rev. Mod. Phys.* **80**, 517-576 (2008).
18. Physically, the transfer of the spin-states to number-states can be accomplished by coherent mapping to photons.
19. Lipkin, H. J., Meshkov, N. & Glick, A. J. Validity of many-body approximation methods for a solvable model. *Nucl. Phys.* **62**, 188-198 (1965).